

# Capturing aromatic Cr<sub>5</sub> pentagons in large main-group molecular cages

Received: 20 April 2024

Accepted: 26 November 2024

Published online: 6 January 2025

 Check for updatesWei-Xing Chen<sup>1,8</sup>, Wen-Juan Tian<sup>2,8</sup>, Zi-Sheng Li<sup>3</sup>, Jing-Jing Wang<sup>2</sup>,  
Alvaro Muñoz-Castro<sup>4</sup>, Gernot Frenking<sup>5,6,7</sup> & Zhong-Ming Sun<sup>1</sup>✉

Chromium chemistry is attractive to researchers due to its interesting structural arrangements and unusual Cr–Cr bonding interactions. However, the exploration of polymeric Cr<sub>n</sub> ( $n > 3$ ) clusters is challenging because of the difficulty in achieving precise matching between the metal cores and ligands. To the best of our knowledge, planar Cr<sub>n</sub> configurations beyond the Cr<sub>3</sub> triangle have not been identified. In this study, we successfully isolated and characterized a Cr<sub>5</sub> cluster using the Zintl ion synthesis route. This cluster exists within the ternary anion [Cr<sub>5</sub>Sn<sub>2</sub>Sb<sub>20</sub>]<sup>4-</sup> and the nanoscale dimer fusion anion [(Cr<sub>5</sub>)<sub>2</sub>Sn<sub>6</sub>Sb<sub>30</sub>]<sup>6-</sup>. Furthermore, we elucidated the aromatic properties of the Cr<sub>5</sub>Sn<sub>2</sub> subunits through theoretical computational analysis, this aromaticity substantially enhancing the intrinsic stability of these Cr<sub>5</sub> cluster species.

Chemical bonding is of fundamental interest in molecular chemistry. Since the groundbreaking discovery of Re–Re complexes featuring multiple bonds<sup>1</sup>, synthetic chemists and theorists have been interested in the study of multiple bonds between transition metals due to their unique bonding properties and electronic structures<sup>2–5</sup>. Among these investigations, binuclear Cr<sub>2</sub> complexes (Fig. 1a), which are typically supported by a variety of organic ligands with diverse coordination modes, have garnered substantial attention, with the primary aim to achieve ultrashort Cr–Cr distances and extreme bond orders<sup>6</sup>. The discovery of a fivefold-bonded Cr<sub>2</sub> dimer has established a benchmark in the field<sup>7</sup>, instigating a surge of research<sup>3,4,8–15</sup>. Numerous theoretical calculations have shown that all of the electrons in the naked Cr<sub>2</sub> dimer spontaneously form a closed-shell system that serves as a building block to form various small Cr<sub>n</sub> ( $n = 3–11$ ) clusters exhibiting unique electronic structures and magnetic properties<sup>16–18</sup>. Unlike theoretical studies, experimental investigations of complexes incorporating Cr–Cr have primarily focused on ligand-supported bimetallic systems, while studies of Cr<sub>n</sub> clusters remain scarce, limiting the exploration of this class of compound and the understanding of Cr–Cr bonding within clusters. Recently, the trichromium complex [(<sup>t</sup>bsL)Cr<sub>3</sub>(thf)] (where <sup>t</sup>bsL

represents 1,3,5-tris[*o*-(*tert*-butyldimethylsilylaminophenyl)amino]cyclohexane and thf denotes tetrahydrofuran; Fig. 1b, top) with multiple active sites has been isolated and found to exhibit promise in small-molecule activation<sup>19,20</sup>. Another notable example involves species containing the octahedral Cr<sub>6</sub> core (Fig. 1b, bottom), belonging to the M<sub>6</sub>E<sub>8</sub>R<sub>6</sub> family (where M = Cr, Mo, Re, Fe; E = S, Se, Te; R = organofunctional group)<sup>21–27</sup>. Based on the existing isolated Cr<sub>n</sub> ( $n = 2, 3, 6$ ) cluster compounds, it is well established that organic ligands play a crucial role in determining their structure and electronic bonding. With an increasing number of atoms, however, transition metal clusters (for example, Cr<sub>n</sub>) exhibit a proclivity to adopt polyhedral structures rather than adhering to a planar ring geometry due to the instability of the latter<sup>28</sup>. Consequently, this poses a challenge for the experimental synthesis of chromium clusters, particularly those featuring planar configurations.

In contrast, there is considerable research activity in the field of intermetallic clusters. In these clusters, a single metal atom or small cluster from the *d* or *f* block of the periodic table is encapsulated within cages formed by *p*-block (semi)metal atoms<sup>29</sup>. So far, a diverse range of clusters containing single or multiple interstitial transition metal atom(s) have been successfully isolated from the reaction of Zintl

<sup>1</sup>State Key Laboratory of Elemento-Organic Chemistry, Tianjin Key Lab of Rare Earth Materials and Applications, School of Material Science and Engineering, Nankai University, Tianjin, China. <sup>2</sup>Institute of Molecular Science, Shanxi University, Taiyuan, China. <sup>3</sup>Department of Chemistry, University of Oxford, Oxford, UK. <sup>4</sup>Facultad de Ingeniería, Arquitectura y Diseño, Universidad San Sebastián, Santiago, Chile. <sup>5</sup>Institute of Advanced Synthesis, School of Chemistry and Molecular Engineering, State Key Laboratory of Materials-Oriented Chemical Engineering, Nanjing Tech University, Nanjing, China. <sup>6</sup>Fachbereich Chemie, Philipps-Universität Marburg, Marburg, Germany. <sup>7</sup>Donostia International Physics Center (DIPC), Donostia, Spain. <sup>8</sup>These authors contributed equally: Wei-Xing Chen, Wen-Juan Tian. ✉e-mail: [sunlab@nankai.edu.cn](mailto:sunlab@nankai.edu.cn)

precursors with organic transition metal precursors<sup>30,31</sup>. Moreover, specific anionic clusters incorporating small planar transition metal fragments  $M_n$  ( $M = \text{Au, Pd, Fe, } n = 3; M = \text{Cu, } n = 4$ ) have been experimentally observed<sup>32–38</sup>. Hence, the strategy of constructing anionic ligands with larger cages from Zintl ions is anticipated to facilitate the encapsulation of small or even metastable planar  $\text{Cr}_n$  ( $n > 2$ ) clusters. Despite the ongoing research endeavours surrounding these compounds, however, the design and synthesis of platforms that allow for the capture of large metastable chromium cluster species remains unrealized.

In this study, we synthesized two Cr clusters,  $[\text{Cr}_5\text{Sn}_2\text{Sb}_{20}]^{4-}$  and  $[(\text{Cr}_5)_2\text{Sn}_6\text{Sb}_{30}]^{6-}$ , by the Zintl ion route under facile and controllable conditions (Fig. 1c). X-ray diffraction analysis showed that the planar  $\text{Cr}_5$  array resides in a pentagonal-bipyramidal  $\text{Cr}_5\text{Sn}_2$  core surrounded by a pure Sb or mixed Sn–Sb molecular cage, forming metal anions of the  $\text{Cr}_5\text{Sn}_2$  monomer and fusion-grown dimer, respectively. The existence of the cyclic  $\text{Cr}_5$  plane was experimentally confirmed through the isolation of the  $[\text{Cr}_5\text{Sn}_2\text{Sb}_{20}]^{4-}$  and  $[(\text{Cr}_5)_2\text{Sn}_6\text{Sb}_{30}]^{6-}$  clusters. This success is attributed to the formation of the aromatic pentagonal-bipyramidal  $\text{Cr}_5\text{Sn}_2$  centre, which may be the key intrinsic factor improving the relative stability of the  $\text{Cr}_5$  array. These findings open a new horizon in the study of chromium cluster chemistry and to the further construction of models for understanding Cr–Cr and Cr–metal bonding.

## Synthesis and characterization

### Synthesis of compounds 1 and 2

The cluster  $[\{\text{K}(\text{18-crown-6})\}_2\text{Cp}\}_4[\text{Cr}_5\text{Sn}_2\text{Sb}_{20}]$  (**1a**) was prepared by treating an ethane-1,2-diamine (en) solution of the ternary Zintl precursor  $\text{K}_8\text{SnSb}_4$  with dicyclopentadienyl chromium ( $\text{CrCp}_2$ ) under heating in the presence of 1,4,7,10,13,16-hexaoxacyclooctadecane (18-crown-6). Following the synthesis of complex **1a**,  $\text{CrCp}_2$  was treated with a solution of precursor  $\text{K}_8\text{SnSb}_4$  in en in the presence of 4,7,13,16,21,24-hexaoxa-1,10-diazabicyclo[8.8.8]hexacosane (2.2.2-crypt) to produce the cluster  $[\text{Cr}_5\text{Sn}_2\text{Sb}_{20}]^{4-}$  as its  $[\text{K}(2.2.2\text{-crypt})]^+$  salt,  $[\text{K}(2.2.2\text{-crypt})]_4[\text{Cr}_5\text{Sn}_2\text{Sb}_{20}]$  (**1b**). With the intention of delving deeper into the reactivity of this system, the fusion dimer product  $[\{\text{K}(\text{18-crown-6})\}_2\text{Cp}\}_2[\text{K}(\text{18-crown-6})]_4[(\text{Cr}_5)_2\text{Sn}_6\text{Sb}_{30}]\text{-en}_4$  (**2**) was obtained by continuously stirring the heated reaction solution at room temperature, following the synthesis route used for compound **1a**. To further verify the relationship between the anions  $[\text{Cr}_5\text{Sn}_2\text{Sb}_{20}]^{4-}$  and  $[(\text{Cr}_5)_2\text{Sn}_6\text{Sb}_{30}]^{6-}$  within the two aforementioned compounds, we heated an en solution of compound **1a** in the presence of the  $\text{K}_8\text{SnSb}_4$  precursor. By employing identical methods, we successfully isolated crystals of compound **2** from the resulting solution. This discovery suggests that the  $[\text{Cr}_5\text{Sn}_2\text{Sb}_{20}]^{4-}$  monomer may act as a viable intermediate in solution, facilitating the formation of nanoscale dimer clusters of  $[(\text{Cr}_5)_2\text{Sn}_6\text{Sb}_{30}]^{6-}$  through a sophisticated assembly process. The synthesis of these complexes has introduced chromium clusters into the Zintl ion system, breaking through the traditional construction strategy for  $\text{Cr}_n$ -containing compounds. To the best of our knowledge, the structures of Cr-related Zintl clusters are relatively simple: most are  $\text{Cr}(\text{CO})_n$  ( $n = 3$  or  $5$ ) fragments acting as electron acceptors bound to the corresponding anions through simple coordination<sup>39–47</sup>, while another example is a  $\text{Cr}_2$  dimer stabilized by a cyclic polyantimony anion<sup>48</sup>. The formation of fusion product **2** can be viewed as an oxidative coupling of two units of cluster **1a**, and thus a controllable aggregation to a larger two-dimensional array of **1a** can be envisaged.

### Characterization

Crystals **1a**, **1b** and **2** were structurally characterized by single-crystal X-ray diffraction (SC-XRD). Complexes **1a** and **1b** crystallize in the orthorhombic space group  $P2_12_12$  and the monoclinic space group  $P2_1/c$ , respectively (Supplementary Figs. 2 and 4). The cluster  $[\text{Cr}_5\text{Sn}_2\text{Sb}_{20}]^{4-}$  crystallizes with 18-crown-6 (in **1a**) and 2.2.2-crypt (in **1b**) as cation-sequestering agents; the former exhibits extensive disorder, whereas in the latter, the degree of disorder is significantly reduced,

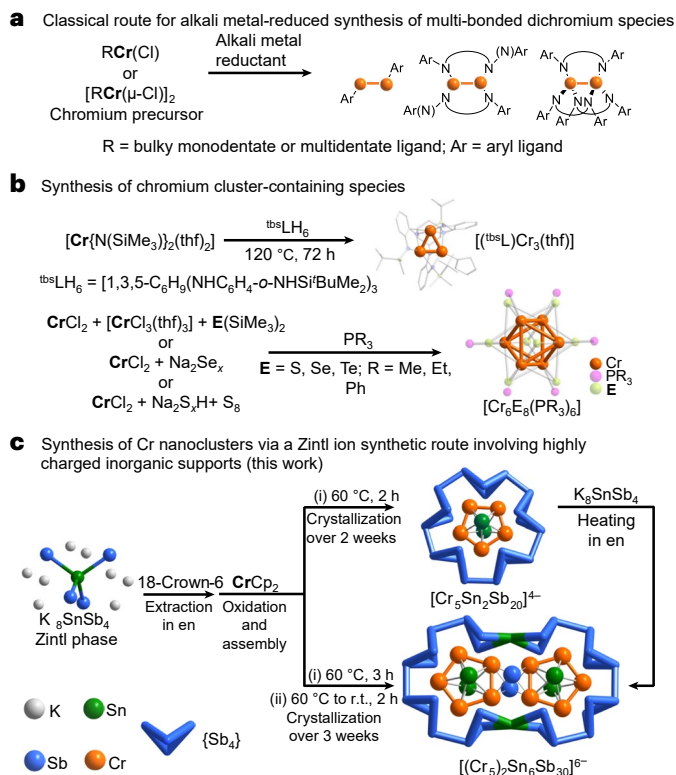


**Fig. 1 | Synthesis of multi-bonded dichromium and chromium cluster-containing species using different synthetic strategies.** **a**, A classical route for the synthesis of multi-bonded dichromium compounds supported by organic ligands using an alkali metal reductant. **b**, Synthetic routes to currently known chromium cluster compounds supported by organic ligands. **c**, This work: two planar  $\text{Cr}_5$  clusters surrounded by inorganic anionic cages were prepared by a Zintl ion synthetic route involving a highly charged inorganic reducing support. r.t., room temperature.

with only slight disorder observed in the anion moieties. Therefore, the following discussion on the structure of the  $[\text{Cr}_5\text{Sn}_2\text{Sb}_{20}]^{4-}$  anion is mainly based on that in compound **1b**. In the solid-state structure of  $[\text{Cr}_5\text{Sn}_2\text{Sb}_{20}]^{4-}$ , the nearly planar  $\text{Cr}_5$  unit combines with five surrounding  $\text{Sb}_2$  dumb-bells in the same horizontal plane, forming a larger equatorial plane denoted  $\text{Cr}_5(\text{Sb}_2)_5$ , while the  $\text{Cr}_5\text{Sn}_2$  core resides in a cage created by a framework comprising 20 Sb atoms (Fig. 2a). The polyanionic  $\text{Sb}_{20}$  unit can be viewed as a large pentamer cage, namely,  $(\text{Sb}_4)_5$ , formed by butterfly-shaped  $\text{Sb}_4$  subunits via *exo*-Sb–Sb bonds. This larger polyatomic cage can also be viewed as a further expansion of the middle-sized  $(\text{Sb}_4)_3^{6-}$  and  $(\text{Bi}_4)_3^{8-}$  units in the clusters  $[\text{Ln}@\text{Sb}_{12}]^{3-}$  (ref. 49),  $[\text{U}@\text{Bi}_{12}]^{3-}$  (ref. 50) and  $[\text{Th}@\text{Bi}_{12}]^{4-}$  (ref. 51). The characterized  $\text{Sb}_{20}$  outer backbone differs from the dodecahedral shape observed in the  $\text{Sb}@\text{Pd}_{12}@\text{Sb}_{20}$  cluster<sup>52</sup>, revealing the flexibility of the architecture of  $\text{Sb}_{20}$  encapsulating different metal cores.

Complex **2** crystallizes in the orthorhombic space group  $Pbcn$ . The asymmetric unit of **2** contains one  $[(\text{Cr}_5)_2\text{Sn}_6\text{Sb}_{30}]^{6-}$  anion, two  $[\{\text{K}(\text{18-crown-6})\}_2\text{Cp}]^+$  cations and four  $[\text{K}(\text{18-crown-6})\text{en}]^+$  cations, with the cations distributed on both sides of the anion (Fig. 2b and Supplementary Fig. 6). In addition, the unit cell displays an elongated *c* axis (Supplementary Fig. 7), as indicated by its unit cell parameters (Supplementary Table 1). The monomer structure of the anion  $[(\text{Cr}_5)_2\text{Sn}_6\text{Sb}_{30}]^{6-}$  resembles that of  $[\text{Cr}_5\text{Sn}_2\text{Sb}_{20}]^{4-}$  as they both possess a pentagonal-bipyramidal  $\text{Sn}_2\text{Cr}_5$  core.  $[(\text{Cr}_5)_2\text{Sn}_6\text{Sb}_{30}]^{6-}$  can be seen as a formal fusion of two  $[\text{Cr}_5\text{Sn}_2\text{Sb}_{16}]^{4-}$  units in the horizontal direction, sharing two Sb atoms and connected by two additional Sn atoms; it can also be seen as two  $[\text{Cr}_5\text{Sn}_2\text{Sb}_{14}]$  subunits bridged by a  $\text{Sn}_2\text{Sb}_2$  unit (Fig. 2h).

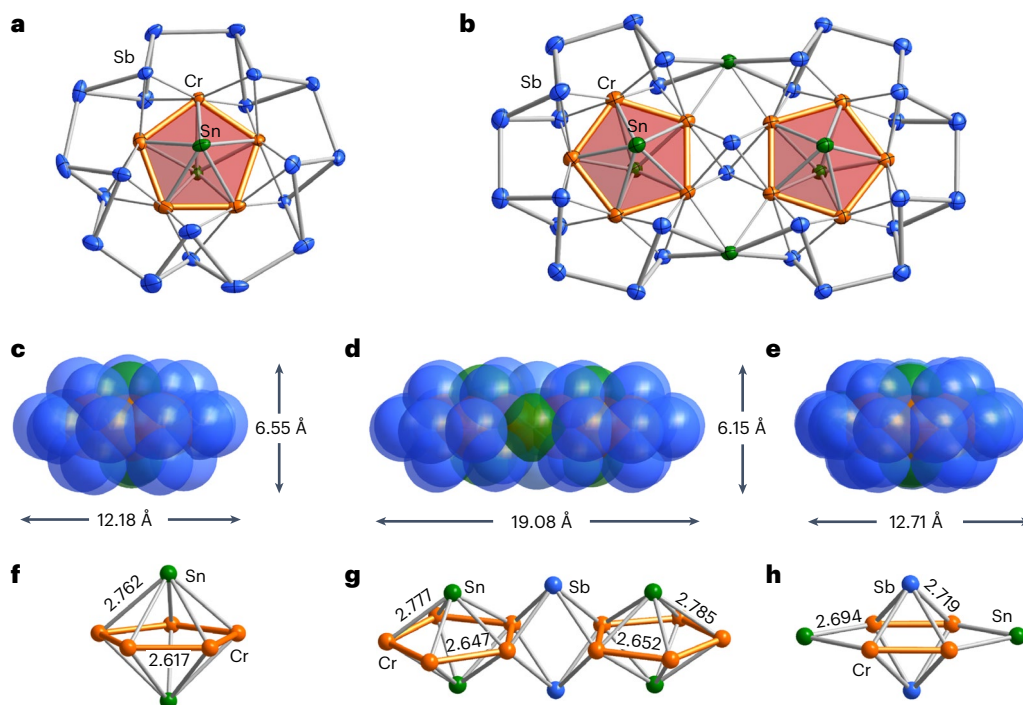


**Fig. 2 | Molecular structures of  $[\text{Cr}_5\text{Sn}_2\text{Sb}_{20}]^{4+}$  and  $[(\text{Cr}_5)_2\text{Sn}_6\text{Sb}_{30}]^{6-}$ .** **a, b**, Top views of  $[\text{Cr}_5\text{Sn}_2\text{Sb}_{20}]^{4+}$  (**a**) and  $[(\text{Cr}_5)_2\text{Sn}_6\text{Sb}_{30}]^{6-}$  (**b**). The ellipsoids are drawn at the 50% probability level; en molecules and the positional disorder of the Sb atoms in  $[\text{Cr}_5\text{Sn}_2\text{Sb}_{20}]^{4+}$  have been omitted for clarity. **c–e**, Side views of  $[\text{Cr}_5\text{Sn}_2\text{Sb}_{20}]^{4+}$  (**c**) and  $[(\text{Cr}_5)_2\text{Sn}_6\text{Sb}_{30}]^{6-}$  (**d, e**). The structures are drawn as space-filling models;

the numbers represent the dimensions (van der Waals lengths) in different directions. **f–h**, The pentagonal-bipyramidal  $\text{Cr}_5\text{Sn}_2$  core in  $[\text{Cr}_5\text{Sn}_2\text{Sb}_{20}]^{4+}$  (**f**) and the  $(\text{Sn}_2\text{CrSb})_2$  (**g**) and  $\text{Cr}_4\text{Sn}_2\text{Sb}_2$  (**h**) fragments in  $[(\text{Cr}_5)_2\text{Sn}_6\text{Sb}_{30}]^{6-}$ . The structures are shown as ball-and-stick models; the average bond lengths are given in ångström.

From an overall structural perspective, similar to  $[\text{Cr}_5\text{Sn}_2\text{Sb}_{20}]^{4+}$ , the two  $\text{Cr}_5$  planes in  $[(\text{Cr}_5)_2\text{Sn}_6\text{Sb}_{30}]^{6-}$ , which are connected by  $\eta^4$ -Sb atoms (Fig. 2g), are encompassed within a larger  $\text{Sn}_2\text{Sb}_{28}$  heterometallic ring. As illustrated in Fig. 2b, the two  $\text{Cr}_5$  rings interconnected by Sb atoms are positioned adjacent to each other and aligned in a parallel manner within the macrocycle. Moreover, the distinct separation of the two  $\text{Cr}_5$  units, as evidenced by the elongated Cr–Cr distance ( $\sim 3.0$  Å), clearly indicates the absence of any significant bonding interactions between them.

The Cr–Cr bond lengths in  $[\text{Cr}_5\text{Sn}_2\text{Sb}_{20}]^{4+}$  (2.544(6)–2.622(7) Å in **1a** and 2.547(3)–2.650(3) Å in **1b**) are slightly shorter than those in  $[(\text{Cr}_5)_2\text{Sn}_6\text{Sb}_{30}]^{6-}$  (2.619(4)–2.674(4) Å), but significantly exceed those in  $[\text{Cr}_2\text{Sb}_{12}]^{3-}$  (2.32 Å) and other organic ligand-supported multi-bonded Cr–Cr complexes<sup>3,7,10–15</sup>. In cluster  $[\text{Cr}_5\text{Sn}_2\text{Sb}_{20}]^{4+}$ , the Cr–Sn bond length (average 2.762 Å) for the capping Sn atoms to the planar  $\text{Cr}_5$  subunit is slightly shorter than that in  $[(\text{Cr}_5)_2\text{Sn}_6\text{Sb}_{30}]^{6-}$  (average 2.780 Å). In contrast, the Cr–Sn bond within the centrally linked  $\text{Sn}_2\text{Sb}_2\text{Cr}_4$  moiety (Fig. 2h) of the  $[(\text{Cr}_5)_2\text{Sn}_6\text{Sb}_{30}]^{6-}$  cluster is relatively short (average 2.694 Å) and the Cr–Sb bond (average 2.719 Å) in this unit is also shorter than the Cr–Sb bonds in other moieties (average 2.745 Å). The Sn–Sb distances between the capping Sn atoms on the central  $\text{Cr}_5$  ring and the surrounding Sb atoms are longer than  $\sim 3.2$  Å, indicating that these Sn atoms prefer to form a closed deltahedral  $\text{Cr}_5\text{Sn}_2$  cluster with the  $\text{Cr}_5$  plane rather than a continuous shell with the  $\text{Sb}_{20}$  or  $\text{Sn}_2\text{Sb}_{28}$  ring, as in the  $\text{Sn}_8\text{Bi}_6$  shell in  $[\text{Pd}_3\text{Sn}_8\text{Bi}_6]^{4+}$  (ref. 34). It is interesting to note that the van der Waals size of the cluster changes substantially during the growth and fusion of the clusters, expanding horizontally from  $\sim 12.18$  Å to  $\sim 19.08$  Å, while experiencing a vertical compression from  $\sim 6.55$  Å to  $\sim 6.15$  Å (Fig. 2c–e).

The compositions of complexes **1** and **2** were rationalized by electrospray ionization mass spectrometry (ESI-MS; Supplementary Fig. 8) and energy-dispersive X-ray (EDX) spectroscopy (Supplementary Figs. 14–16). ESI-MS of **1a** was performed in acetonitrile solution

and displayed peaks arising from  $[\text{Sn}_2\text{Cr}_5\text{Sb}_{18}]^{2-}$  ( $m/z = 1,344.8620$ ),  $[\text{K}(18\text{-crown-6})\text{Sn}_2\text{Cr}_5\text{Sb}_{18}]^{2-}$  ( $m/z = 1,496.4176$ ) and other related fragmentation peaks (Supplementary Figs. 9–13). Under ESI-MS gas-phase conditions, the parent anion  $[\text{Cr}_5\text{Sn}_2\text{Sb}_{20}]^{4-}$  lost two Sb atoms, resulting in the prominent peak of  $[\text{Sn}_2\text{Cr}_5\text{Sb}_{18}]^{2-}$ , indicating that the parent anion was unstable to the analytical conditions. Furthermore, crystalline samples of **1a** analysed by electron paramagnetic resonance (EPR) spectroscopy showed a single paramagnetic signal with a central  $g$ -value of 2.042, confirming its paramagnetic nature (Supplementary Fig. 17). Theoretical calculations revealed that the ground state of the  $[\text{Cr}_5\text{Sn}_2\text{Sb}_{20}]^{4-}$  cluster has a spin state  $S = 1$ , with two unpaired electrons distributed across the atoms of the  $\text{Cr}_5$  plane. For compound **2**, despite many attempts, we were unable to obtain pertinent and valid data from ESI-MS and EPR experiments, suggesting the inherent instability of the compound under the test conditions.

### Theoretical analysis

Next, we carried out a theoretical analysis to further rationalize the chemical bonding and related characteristics of the  $[\text{Cr}_5\text{Sn}_2\text{Sb}_{20}]^{4+}$  and  $[(\text{Cr}_5)_2\text{Sn}_6\text{Sb}_{30}]^{6-}$  clusters. The favoured spin state for such species was verified using the Perdew–Burke–Ernzerhof (PBE) functional to range from  $S = 0$  to  $S = 2$ , indicating that  $S = 1$  is preferred for  $[\text{Cr}_5\text{Sn}_2\text{Sb}_{20}]^{4+}$  and  $[(\text{Cr}_5)_2\text{Sn}_6\text{Sb}_{30}]^{6-}$  (Supplementary Table 4). Interestingly, for  $[(\text{Cr}_5)_2\text{Sn}_6\text{Sb}_{30}]^{6-}$ , the favoured optimized structure with  $S = 1$  deviates significantly from the experimental SC-XRD structure, while the structural parameters with  $S = 2$  closely approximate the experimental data (Supplementary Table 6). Thus, the quintet state ( $S = 2$ ) was further evaluated as it better accounts for the electronic ground state found in the experimentally characterized  $[(\text{Cr}_5)_2\text{Sn}_6\text{Sb}_{30}]^{6-}$  cluster. This discrepancy between the electronic ground state and the experimental results for  $[(\text{Cr}_5)_2\text{Sn}_6\text{Sb}_{30}]^{6-}$  may also manifest in certain high-nuclear clusters<sup>53,54</sup>. To estimate the separation of the frontier orbitals in the characterized clusters, we evaluated the gap between the highest-occupied

and lowest-unoccupied molecular orbitals (the HOMO–LUMO gap) for the  $S = 0$  spin state. HOMO–LUMO gaps of 0.78 and 0.88 eV were obtained for  $[\text{Cr}_5\text{Sn}_2\text{Sb}_{20}]^{4+}$  and  $[(\text{Cr}_5)_2\text{Sn}_6\text{Sb}_{30}]^{6-}$ , respectively, suggesting a semiconductor-like behaviour for such species, as is often found for Zintl ions<sup>55</sup>.

Furthermore, we used canonical molecular orbital analysis at the PBE0/def2-tzvp level and adaptive natural density partitioning (AdNDP) analysis to elucidate the chemical bonding. The optimized structures demonstrate Cr–Cr bond lengths in  $[\text{Cr}_5\text{Sn}_2\text{Sb}_{20}]^{4+}$  of 2.515–2.639 Å and in  $[(\text{Cr}_5)_2\text{Sn}_6\text{Sb}_{30}]^{6-}$  of 2.667–2.792 Å, in close agreement with the experimental SC-XRD values (2.539(6)–2.650(3) Å for the former and 2.615(4)–2.676(4) Å for the latter), supporting the spin states evaluated for these species. The results of the AdNDP analysis for  $[\text{Cr}_5\text{Sn}_2\text{Sb}_{20}]^{4+}$  show one centre–two electron (1c–2e) lone-pair electrons (20 Sb 5s lone pairs, 5 Cr 4s lone pairs and 2 Sn 5s lone pairs), 2c–2e  $\sigma$  bonds (5 Cr–Cr  $\sigma$  bonds in the  $\text{Cr}_5$  ring and 25 Sb–Sb  $\sigma$  bonds in the outer  $\text{Sb}_{20}$  skeleton) and a specific type of 3c–2e  $\sigma$  bond (10 Cr–Sb–Cr  $\sigma$  bonds) that complete the bonding picture within the  $\text{Cr}_5\text{Sn}_2$  core and the outer  $\text{Sb}_{20}$  skeleton. Moreover, three core delocalized 7c–2e  $\sigma$  bonds in the  $\text{Cr}_5\text{Sn}_2$  unit and two global delocalized 27c–1e electrons distributed throughout the overall cluster account for the remaining eight electrons (Supplementary Fig. 19). Notably, the set of three 7c–2e  $\sigma$  bonds in the  $\text{Cr}_5\text{Sn}_2$  core, amounting to six electrons, adheres to the  $4n + 2$  Hückel rule, revealing the aromatic nature of this unit (Fig. 3). Compared with  $[\text{Cr}_5\text{Sn}_2\text{Sb}_{20}]^{4+}$ , the AdNDP bonding pattern in the  $[(\text{Cr}_5)_2\text{Sn}_6\text{Sb}_{30}]^{6-}$  cluster exhibits subtle variations. The analysis revealed that the 1c–2e lone pairs include 30 Sb 5s lone pairs, 6 Sn 5s lone pairs, 10 Cr 3d lone pairs and 10 Cr 4s lone pairs, while the localized 2c–2e  $\sigma$  bonds consist of 30 Sb–Sb 2c–2e  $\sigma$  bonds in the outer Sb skeleton and 4 Cr–Cr 2c–2e  $\sigma$  bonds in each  $\text{Cr}_5$  ring. Thus, the bonding in the  $\text{Cr}_5$  ring differs from that observed in  $[\text{Cr}_5\text{Sn}_2\text{Sb}_{20}]^{4+}$ , which features five Cr–Cr  $\sigma$  bonds. In  $[(\text{Cr}_5)_2\text{Sn}_6\text{Sb}_{30}]^{6-}$ , the absence of these individual bonds enables the formation of four 3c–2e Cr–Sb–Cr  $\sigma$  bonds (occupation numbers (ON) = 1.75 |e|) connecting the two  $\text{Cr}_5$  units, representing a judicious allocation of electrons crucial for the stability of the overall structure. In addition, 16 3c–2e  $\sigma$  bonds, involving 8 Cr–Sb–Cr  $\sigma$  bonds and 8 Cr–Sb–Sn  $\sigma$  bonds, intricately connect the two inner  $\text{Cr}_5\text{Sn}_2$  units to the outer  $\text{Sn}_2\text{Sb}_{28}$  skeleton. Two delocalized 7c–2e  $\sigma$  bonds and one 7c–1e electron in each  $\text{Cr}_5\text{Sn}_2$  unit as well as two global delocalized 46c–1e electrons account for the remaining 12 electrons in the system (Supplementary Fig. 20). Remarkably, the presence of six electrons in each  $\text{Cr}_5\text{Sn}_2$  unit in both  $[\text{Cr}_5\text{Sn}_2\text{Sb}_{20}]^{4+}$  and  $[(\text{Cr}_5)_2\text{Sn}_6\text{Sb}_{30}]^{6-}$ , reveals that the aromatic motif has been preserved in the building block unit during the fusion process (Fig. 3). This unique property might play a crucial role in maintaining the overall stability of these clusters, particularly in larger fused structures, as found here.

To further evaluate the aromatic properties of the  $\text{Cr}_5\text{Sn}_2$  core in the characterized clusters  $[\text{Cr}_5\text{Sn}_2\text{Sb}_{20}]^{4+}$  and  $[(\text{Cr}_5)_2\text{Sn}_6\text{Sb}_{30}]^{6-}$ , we calculated the nucleus-independent chemical shift accounting for an applied field oriented perpendicular to the  $\text{Cr}_5$  ring plane (NICS<sub>zz</sub>). The NICS<sub>zz</sub> values at the centre of the  $\text{Cr}_5\text{Sn}_2$  core in these two new clusters were calculated to be –8.96 and –30.97 ppm, respectively, consistent with the aromatic nature of the system core. These values reveal an enhancement of the shielding region in the dimer structure due to the extension of the shielding region through the fusion of the two units. In addition, the overall aromatic nature of  $[\text{Cr}_5\text{Sn}_2\text{Sb}_{20}]^{4+}$  and  $[(\text{Cr}_5)_2\text{Sn}_6\text{Sb}_{30}]^{6-}$  is further evidenced by their isochemical shielding surfaces (ICSSs; Fig. 4). These findings underscore that the aromatic properties of these systems primarily emanate from the inner  $\text{Cr}_5\text{Sn}_2$  core and extend to the overall cluster structure in both the monomer and dimer forms as an inorganic all-metal cluster counterpart of cyclopentadienide ( $\text{Cp}^-$ ) and its fused-ring derivatives such as cyclobuta[1,2,3,4]dicyclopentene<sup>56</sup>.

To elucidate the bonding interactions between the cluster core ( $\text{Cr}_5\text{Sn}_2$  in  $[\text{Cr}_5\text{Sn}_2\text{Sb}_{20}]^{4+}$  and  $[(\text{Cr}_5)_2\text{Sn}_6\text{Sb}_{30}]^{6-}$ ) and the surrounding pure Sb or mixed Sn–Sb molecular cages in the two

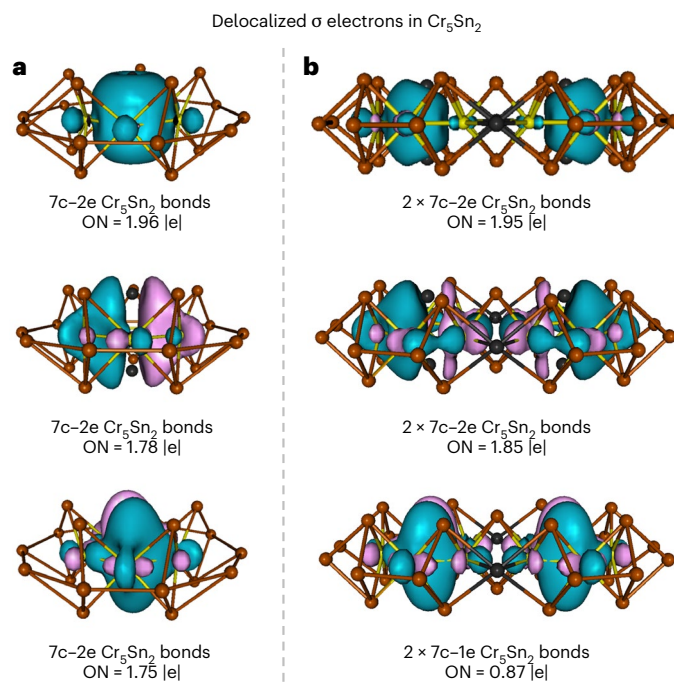


**Fig. 3** | AdNDP bonding patterns in  $[\text{Cr}_5\text{Sn}_2\text{Sb}_{20}]^{4+}$  and  $[(\text{Cr}_5)_2\text{Sn}_6\text{Sb}_{30}]^{6-}$ . **a**, Three local delocalized 7c–2e  $\sigma$  bonds in the internal  $\text{Cr}_5\text{Sn}_2$  motif of  $[\text{Cr}_5\text{Sn}_2\text{Sb}_{20}]^{4+}$ . **b**, Four local delocalized 7c–2e and two 7c–1e  $\sigma$  bonds in the internal  $\text{Cr}_5\text{Sn}_2$  motifs of  $[(\text{Cr}_5)_2\text{Sn}_6\text{Sb}_{30}]^{6-}$ .

clusters, we performed an energy decomposition analysis (EDA). The fragmentation interactions of the clusters  $[\text{Cr}_5\text{Sn}_2\text{Sb}_{20}]^{4+}$  and  $[(\text{Cr}_5)_2\text{Sn}_6\text{Sb}_{30}]^{6-}$  in different charge states were calculated (Table 1 and Supplementary Tables 2 and 3). In the  $[\text{Cr}_5\text{Sn}_2\text{Sb}_{20}]^{4+}$  system, the  $[\text{Sb}_{20}]^{6-}$  and  $[\text{Sn}_2\text{Cr}_5]^{2+}$  fragments were identified as optimal for elucidating the bonding between the central core and the anionic ligand, with an orbital interaction ( $\Delta E_{\text{orb}}$ ) of –1,078.6 kcal mol<sup>–1</sup>. Within this context, the fragments demonstrated a binding energy ( $\Delta E_{\text{int}}$ ) of –1,074.2 kcal mol<sup>–1</sup>, with electrostatic interactions (64%) exerting a more pronounced influence than covalent interactions (36%), primarily due to the lower degree of electron transfer between the fragments. In the case of  $[(\text{Cr}_5)_2\text{Sn}_6\text{Sb}_{30}]^{6-}$ , the results in Table 1 reveal that the interaction between the  $[\text{Sn}_2\text{Sb}_{28}]^{8-}$  and  $[(\text{Sn}_2\text{Cr}_5)\text{Sb}]_2^{2+}$  fragments provides the most accurate description of the bonding scheme. The binding energy between these fragments is –1,398.0 kcal mol<sup>–1</sup>, with electrostatic interactions (62%) prevailing over covalent interactions (38%) due to reduced orbital overlap. Moreover, steric hindrance is primarily attributed to Pauli repulsion ( $\Delta E_{\text{Pauli}}$ ). In both clusters, electrostatic interactions dominate the cluster stabilization, which to some extent is indicative of their ionic nature.

Electron density difference analysis revealed the interactions between the core and shell fragments and the directional flow of electrons from the core to the outer skeleton (Supplementary Figs. 21 and 22). The contributions of both the core and outer fragments of  $[\text{Cr}_5\text{Sn}_2\text{Sb}_{20}]^{4+}$  and  $[(\text{Cr}_5)_2\text{Sn}_6\text{Sb}_{30}]^{6-}$  to the molecular orbitals (MOs) are shown in detail in Supplementary Fig. 23. Notably, the overall energy distributions of the orbitals in both clusters are consistent, with similar relative contributions from the fragments in each system. The results of the density of states analysis (Supplementary Fig. 23), combined with the AdNDP and EDA findings, reveal the crucial contribution of the aromatic  $\text{Cr}_5\text{Sn}_2$  units to the overall stability. Calculation of the Voronoi and Hirshfeld charges gave the expected values (Supplementary Tables 7 and 8), with the highly negatively charged cluster having a charge distribution similar to a Faraday cage, contributing to the overall aromatic properties evidenced by the ICSSs (Fig. 4).

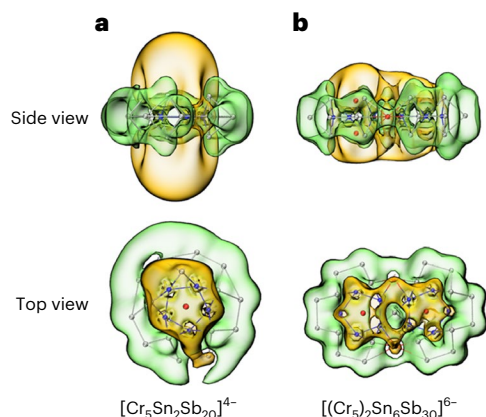


**Fig. 4** | Calculated ICSSs of  $[\text{Cr}_5\text{Sn}_2\text{Sb}_{20}]^{4-}$  and  $[(\text{Cr}_5)_2\text{Sn}_6\text{Sb}_{30}]^{6-}$ . **a, b**, Top and side views of  $[\text{Cr}_5\text{Sn}_2\text{Sb}_{20}]^{4-}$  (**a**) and  $[(\text{Cr}_5)_2\text{Sn}_6\text{Sb}_{30}]^{6-}$  (**b**). The yellow and green regions correspond to negative and positive ICSS values, respectively. ICSS isosurface =  $\pm 7$  ppm.

**Table 1** | Results of the EDA of  $[\text{Cr}_5\text{Sn}_2\text{Sb}_{20}]^{4-}$  and  $[(\text{Cr}_5)_2\text{Sn}_6\text{Sb}_{30}]^{6-}$  at the PBE/TZ2P-ZORA level

	$[\text{Cr}_5\text{Sn}_2\text{Sb}_{20}]^{4-}$ (triplet)	$[(\text{Cr}_5)_2\text{Sn}_6\text{Sb}_{30}]^{6-}$ (quintet)
Interacting fragments	$[\text{Sn}_2\text{Cr}_5]^{2+}-[\text{Sb}_{20}]^{6-}$	$\{[(\text{Sn}_2\text{Cr}_5)\text{Sb}]_2\}^{2+}-[\text{Sn}_2\text{Sb}_{28}]^{8-}$
$\Delta E_{\text{int}}$ (kcal mol <sup>-1</sup> )	-1,074.2	-1,398.0
$\Delta E_{\text{Pauli}}$ (kcal mol <sup>-1</sup> )	+1,921.5	+3,917.2
$\Delta E_{\text{elstat}}$ (kcal mol <sup>-1</sup> ) <sup>a</sup>	-1,920.0 (64)	-3,314.0 (62)
$\Delta E_{\text{orb}}$ (kcal mol <sup>-1</sup> ) <sup>a</sup>	-1,078.6 (36)	-2,001.2 (38)

<sup>a</sup>The values in parentheses represent the percentage contribution to the total attractive interactions:  $\Delta E_{\text{elstat}}$  (the electrostatic interaction) +  $\Delta E_{\text{orb}}$  (the orbital interaction). TZ2P, triple- $\xi$  plus the double-polarization; ZORA, zeroth-order regular approximation.

The favoured triplet spin state for  $[\text{Cr}_5\text{Sn}_2\text{Sb}_{20}]^{4-}$  and quintet spin state for  $[(\text{Cr}_5)_2\text{Sn}_6\text{Sb}_{30}]^{6-}$  suggest ferromagnetic coupling between spins within the overall cluster structure. To explore the location of the unpaired electrons, we calculated the respective spin density isosurfaces. The results show that the unpaired electrons predominantly reside at the Cr centres in the  $\text{Cr}_5$  rings, without substantial sharing with the outer  $\text{Sb}_{20}$  or  $\text{Sb}_{30}$  framework or the apical Sn atoms (Supplementary Fig. 24). Thus, variation of the composition of the  $\text{M}_5$  rings could be useful for modifying the spin-state characteristics by incorporating paramagnetic or diamagnetic transition metal centres. Therefore, the characterized  $[\text{Cr}_5\text{Sn}_2\text{Sb}_{20}]^{4-}$  and  $[(\text{Cr}_5)_2\text{Sn}_6\text{Sb}_{30}]^{6-}$  clusters can be viewed as useful platforms for identifying different isostructural paramagnetic clusters.

## Conclusion

We have synthesized and characterized the anionic clusters  $[\text{Cr}_5\text{Sn}_2\text{Sb}_{20}]^{4-}$  and  $[(\text{Cr}_5)_2\text{Sn}_6\text{Sb}_{30}]^{6-}$  featuring planar  $\text{Cr}_5$  motifs. The monomer species underwent useful aggregation through oxidative coupling to form dimer species, allowing the further connection of several units in a two-dimensional array to be envisaged. The planar  $\text{Cr}_5$  unit in the clusters collaborates with two Sn atoms on either side of the plane, forming a pentagonal-bipyramidal polyhedral  $\text{Cr}_5\text{Sn}_2$  core embedded in a substantial metal cage composed of pure Sb or binary Sn–Sb. In addition, the outer  $\text{Sb}_{20}$  backbone can adopt an open-shell configuration, in contrast to the dodecahedral contour of  $\text{Sb}@\text{Pd}_{12}@\text{Sb}_{20}$  clusters. Theoretical calculations elucidated the unique aromaticity inherent in the  $\text{Cr}_5\text{Sn}_2$  core, representing a crucial element for the stable existence of both the planar  $\text{Cr}_5$  motif and the entire anionic cluster. In addition, these species can be seen as inorganic all-metal counterparts of the organic cyclopentadienyl ( $\text{Cp}^-$ ) aromatic ring and its fused derivatives. The discovery of planar  $\text{Cr}_5$  in these synthetic

clusters has expanded the research scope of chromium chemistry, offering a model for investigating metal–metal bonding and inspiring new research avenues for the design and synthesis of this series of species, encouraging the preparation of other clusters with variable spin states featuring isostructural characteristics.

## Methods

All manipulations and reactions were performed under a  $\text{N}_2$  atmosphere using standard Schlenk or glove-box techniques. The solvents en (Aldrich, 99%) and toluene (Aldrich, 99.8%) were freshly distilled from sodium–benzophenone. Acetonitrile (Aldrich, 99.8%) and *N,N*-dimethylformamide (Aldrich, 99.8%) were distilled from  $\text{CaH}_2$  under  $\text{N}_2$  and stored under  $\text{N}_2$  before use. 2.2.2-Crypt (Sigma-Aldrich, 98%) and 18-crown-6 (Sigma-Aldrich, 98%) were dried under vacuum for 1 day before use. The precursor  $\text{K}_8\text{SnSb}_4$  was synthesized from a stoichiometric mixture of the elements according to a previously reported synthetic procedure<sup>57</sup>.  $\text{CrCp}_2$  was synthesized following a literature procedure<sup>58</sup>.

### Synthesis of $[\{\text{K}(\text{18-crown-6})\}_2\text{Cp}]_4[\text{Cr}_5\text{Sn}_2\text{Sb}_{20}]$ (**1a**)

In a 10 ml vial,  $\text{K}_8\text{SnSb}_4$  (92 mg, 0.100 mmol) and 18-crown-6 (98 mg, 0.370 mmol) were dissolved in 2.5 ml en and stirred at 50 °C for 0.5 h to yield a brown solution.  $\text{CrCp}_2$  (30 mg, 0.165 mmol) was added slowly to this mixture over 0.5 h and then stirred vigorously at 60 °C for 2 h. The mixture was centrifuged and the liquid supernatant transferred to a test tube, then carefully layered with toluene (3.0 ml) to allow for crystallization. After 2 weeks, black block crystals of **1a** were observed in the test tube with a yield of -29% (based on  $\text{CrCp}_2$ ).

### Synthesis of $[\{\text{K}(\text{2.2.2-crypt})\}_4[\text{Cr}_5\text{Sn}_2\text{Sb}_{20}]$ (**1b**)

In a 10 ml vial,  $\text{K}_8\text{SnSb}_4$  (92 mg, 0.100 mmol) and 2.2.2-crypt (115 mg, 0.305 mmol) were dissolved in 2.5 ml en and stirred at 50 °C for 0.5 h to yield a brown solution.  $\text{CrCp}_2$  (23 mg, 0.127 mmol) was added slowly to this mixture over 0.5 h and then stirred vigorously at 70 °C for 3 h. The mixture was centrifuged and the liquid supernatant transferred to a test tube, then carefully layered with toluene (3.0 ml) to allow for crystallization. After 3 weeks, black block crystals of **1b** were observed in the test tube with a yield of -18% (based on  $\text{CrCp}_2$ ).

### Synthesis of $[\{\text{K}(\text{18-crown-6})\}_2\text{Cp}]_2[\text{K}(\text{18-crown-6})]_4[(\text{Cr}_5)_2\text{Sn}_6\text{Sb}_{30}]\cdot\text{en}_4$ (**2**)

**Method 1.** In a 10 ml vial,  $\text{K}_8\text{SnSb}_4$  (92 mg, 0.100 mmol) and 18-crown-6 (98 mg, 0.370 mmol) were dissolved in 2.5 ml en and stirred at 50 °C for 0.5 h to yield a brown solution.  $\text{CrCp}_2$  (30 mg, 0.165 mmol) was added slowly to this mixture over 0.5 h and then stirred vigorously at 60 °C for 3 h. Subsequently, the solution was gradually cooled to room temperature with stirring and the reaction allowed to continue for a further 2 h. The mixture was centrifuged and the liquid supernatant transferred to a test tube, then carefully layered with toluene (3.0 ml) to allow for crystallization. After 10 weeks, black flake crystals of **2** were observed in the test tube with a yield of -13% (based on  $\text{CrCp}_2$ ).

**Method 2.** In a 10 ml vial, **1a** (57 mg, 0.001 mmol) and  $\text{K}_8\text{SnSb}_4$  (18 mg, 0.020 mmol) were dissolved in 2.0 ml en to yield a brown solution and then stirred vigorously at 60 °C for 2 h. Subsequently, the solution was gradually cooled to room temperature with stirring and the reaction allowed to continue for a further 2 h. The mixture was centrifuged and the liquid supernatant transferred to a test tube, then carefully layered with toluene (2.0 ml) to allow for crystallization. After 8 weeks, black flake crystals of **2** were observed in the test tube with a yield of -9% (based on **1a**).

**Note.** Small amounts of amorphous solid by-products were generated during the synthesis and crystallization of compounds **1** and **2**, some of which originated from degraded Sn or Sb, while others remained unidentified. Regarding mutual conversion, crystals of both **1** and **2**

may coexist in the same reaction, but only one corresponding compound was observed in each reaction system during the experiments. Furthermore, no evidence was found of compound **2** converting into compound **1** in these experiments.

### SC-XRD analysis

Suitable single crystals of the title compounds were selected for SC-XRD analysis. The crystallographic data were collected on a Rigaku XtalAB Pro MM007 DW diffractometer using graphite-monochromated Cu K $\alpha$  radiation ( $\lambda = 1.54184 \text{ \AA}$ ). The structures of **1a**, **1b** and **2** were solved using direct methods and then refined to convergence using SHELXL-2014 and Olex2 (refs. 59–61), with the non-hydrogen atoms refined anisotropically during the final cycles. All hydrogen atoms of the organic molecule were placed according to geometrical considerations and added to the structure factor calculations. We used the PLATON SQUEEZE procedure to remove solvent molecules that could not be modelled properly<sup>62</sup>. We refined the structure using the rational restraints of anisotropy (SIMU, ISOR and DFIX for K(18-crown-6) fragments) and omitted the most disagreeable reflections. Significant atomic disorder was observed in the Sb<sub>20</sub> portion in compounds **1a** and **1b**. Despite the implementation of the corresponding treatments, the impact of this disorder on atomic statistics could not be fully resolved. In addition, the 18-crown-6 molecule in **1a** exhibits a significant proclivity for disorder, necessitating the treatment of atomic disorder and the implementation of the corresponding constraints. The crystallographic data for the title compounds are summarized in Supplementary Table 1. The crystallographic data for **1a**, **1b** and **2** are freely available from the Cambridge Crystallographic Data Centre under CCDC entries 2212806, 2212807 and 2322476, respectively.

### ESI-MS investigations

Negative ion mode ESI-MS analysis of acetonitrile solutions of crystal samples was performed on an LTQ linear ion trap spectrometer (Agilent ESI time-of-flight mass spectrometer, 6230). The spray voltage was 5.48 kV, the capillary voltage was 30 V and the capillary temperature was 300 °C. Samples were prepared inside a glove box and rapidly transferred to the spectrometer in an airtight syringe by direct infusion with a Harvard syringe pump at 0.2 ml min<sup>-1</sup>.

### EDX analysis

EDX analysis was performed on a field emission scanning electron microscope (JEOL, JSM-7800F). Data acquisition was performed with an acceleration voltage of 15 kV and an accumulation time of 60 s.

### EPR spectroscopy

EPR experiments were carried out using a commercial Bruker ELEXSYS E580 spectrometer (X band, 9 GHz) at 95 K.

### Theoretical methods

**AdNDP analysis.** Canonical molecular orbital analysis, conducted using Gaussian 16 (ref. 63) at the PBE0/def2-tzvp level<sup>64</sup>, and AdNDP<sup>65</sup> analysis were used to elucidate the chemical bonding in the structures. Orbital compositions were analysed using Multiwfn 3.8 (ref. 66).

**EDA analysis.** A detailed EDA analysis<sup>67</sup> was conducted using the Amsterdam Modeling Suite program<sup>68,69</sup> with the all-electron triple- $\zeta$  Slater basis set plus the double-polarization basis set in conjunction with the generalized gradient approximation PBE functional to quantitatively elucidate the interfragmental interactions. The scalar relativistic effect of metals was considered using ZORA<sup>70,71</sup>. The frozen-core approximation was applied to the 1s<sup>2</sup> 4p<sup>6</sup> shells for Sb, the 1s<sup>2</sup> 4p<sup>6</sup> shells for Sn and the 1s<sup>2</sup> 2p<sup>6</sup> shells for Cr, leaving the remaining valence electrons to participate in the interactions. The precision of the spatial integration was set to normal and the wave functions of the  $\alpha$ - and  $\beta$ -electrons for the open shell system were obtained by iteration.

The interaction energy ( $\Delta E_{\text{int}}$ ) between two fragments can be quantitatively decomposed into electrostatic interactions ( $\Delta E_{\text{elstat}}$ ), the Pauli repulsion energy ( $\Delta E_{\text{Pauli}}$ ) and the orbital interaction energy ( $\Delta E_{\text{orb}}$ ):  $\Delta E_{\text{int}} = \Delta E_{\text{Pauli}} + \Delta E_{\text{elstat}} + \Delta E_{\text{orb}}$ .  $\Delta E_{\text{Pauli}}$  refers to the short-range crowding between the occupied orbital of one segment and the occupied orbital of another segment,  $\Delta E_{\text{elstat}}$  represents the attraction of local charges and can be understood as ionic properties, and  $\Delta E_{\text{orb}}$  refers to the interaction between orbitals that leads to charge transfer (sharing), referring to covalence. Fragments with the least energy change during bond formation are the optimal choice to represent the bonding situation objectively. The smallest absolute value of the orbital interaction energy ( $\Delta E_{\text{orb}}$ ) is used as a measure for the most appropriate representation of a molecule when the binding situation is not clear<sup>72,73</sup>.

**Electron density difference analysis.** The parameter settings for the electron density difference analysis were computed using Gaussian 09 (ref. 74) at the PBE0/def2-tzvp level and plotted using Multiwfn<sup>66</sup>.

Solvent and counterion effects were taken into account via the Conductor like Screening Model<sup>75</sup> using en as the solvent in all calculations.

### Data availability

Crystallographic data for the structures reported in this paper have been deposited at the Cambridge Crystallographic Data Centre under deposition numbers CCDC 2212806 (**1a**), 2212807 (**1b**) and 2322476 (**2**) and are freely available via <https://www.ccdc.cam.ac.uk/structures/>. All other data supporting the findings of this study are available within the paper and its Supplementary Information.

### References

1. Cotton, F. A. et al. Mononuclear and polynuclear chemistry of rhenium(III): its pronounced homophilicity. *Science* **145**, 1305–1307 (1964).
2. Cotton, F. A., Murillo, C. A. & Walton, R. A. *Multiple Bonds Between Metal Atoms* (Springer, 2005).
3. Liddle, S. T. *Molecular Metal-Metal Bonds: Compounds, Synthesis, Properties* (Wiley, 2015).
4. Frenking, G. Building a quintuple bond. *Science* **310**, 796–797 (2005).
5. McGrady, J. E. in *Comprehensive Inorganic Chemistry II* 2nd edn (eds Reedijk, J. & Poeppelemeier, K. R.) 321–340 (Elsevier, 2013).
6. Wagner, F. R., Noor, A. & Kempe, R. Ultrashort metal–metal distances and extreme bond orders. *Nat. Chem.* **1**, 529–536 (2009).
7. Nguyen, T. et al. Synthesis of a stable compound with fivefold bonding between two chromium(I) centers. *Science* **310**, 844–847 (2005).
8. Brynda, M., Gagliardi, L., Widmark, P. O., Power, P. P. & Roos, B. O. A quantum chemical study of the quintuple bond between two chromium centers in [PhCrCrPh]: *trans*-bent versus linear geometry. *Angew. Chem. Int. Ed.* **45**, 3804–3807 (2006).
9. Shiozaki, T. & Vlasisavljevich, B. Computational spectroscopy of the Cr–Cr bond in coordination complexes. *Inorg. Chem.* **60**, 19219–19225 (2021).
10. Kreisel, K. A., Yap, G. P. A., Dmitrenko, O., Landis, C. R. & Theopold, K. H. The shortest metal–metal bond yet: molecular and electronic structure of a dinuclear chromium diazadiene complex. *J. Am. Chem. Soc.* **129**, 14162–14163 (2007).
11. Wolf, R. et al. Substituent effects in formally quintuple-bonded ArCrCrAr compounds (Ar = terphenyl) and related species. *Inorg. Chem.* **46**, 11277–11290 (2007).
12. Ashley, A. E., Cooper, R. T., Wildgoose, G. G., Green, J. C. & O'Hare, D. Homoleptic permethylpentalene complexes: 'double metallocenes' of the first-row transition metals. *J. Am. Chem. Soc.* **130**, 15662–15677 (2008).

- Hsu, C. W. et al. Quintuply-bonded dichromium(I) complexes featuring metal–metal bond lengths of 1.74 Å. *Angew. Chem. Int. Ed.* **47**, 9933–9936 (2008).
- Huang, Y.-L. et al. Stepwise construction of the Cr–Cr quintuple bond and its destruction upon axial coordination. *Angew. Chem. Int. Ed.* **51**, 7781–7785 (2012).
- Eisenhart, R. J., Carlson, R. K., Boyle, K. M., Gagliardi, L. & Lu, C. C. Synthesis and redox reactivity of a phosphine-ligated dichromium paddlewheel. *Inorganica Chim. Acta* **424**, 336–344 (2015).
- Cheng, H. & Wang, L.-S. Dimer growth, structural transition, and antiferromagnetic ordering of small chromium clusters. *Phys. Rev. Lett.* **77**, 51–54 (1996).
- Martínez, J. I. & Alonso, J. A. Theoretical study of the photoabsorption spectrum of small chromium clusters. *Phys. Rev. B* **76**, 205409 (2007).
- Ruiz-Díaz, P., Ricardo-Chávez, J. L., Dorantes-Dávila, J. & Pastor, G. M. Magnetism of small Cr clusters: interplay between structure, magnetic order, and electron correlations. *Phys. Rev. B* **81**, 224431 (2010).
- Bartholomew, A. K. et al. Ligand-based control of single-site vs. multi-site reactivity by a trichromium cluster. *Angew. Chem. Int. Ed.* **58**, 5687–5691 (2019).
- Bartholomew, A. K. et al. Revealing redox isomerism in trichromium imides by anomalous diffraction. *Chem. Sci.* **12**, 15739–15749 (2021).
- Taro, S. & Hideo, I. Chalcogenide cluster complexes of chromium, molybdenum, tungsten, and rhenium. *Bull. Chem. Soc. Jpn* **69**, 2403–2417 (1996).
- Gray, T. Hexanuclear and higher nuclearity clusters of the Groups 4–7 metals with stabilizing  $\pi$ -donor ligands. *Coord. Chem. Rev.* **243**, 213–235 (2003).
- Fan, P.-D., Deglmann, P. & Ahlrichs, R. Electron counts for face-bridged octahedral transition metal clusters. *Chem. Eur. J.* **8**, 1059–1067 (2002).
- Bügel, P., Krummenacher, I., Weigend, F. & Eichhöfer, A. Experimental and theoretical evidence for low-lying excited states in  $[\text{Cr}_6\text{E}_6(\text{PET}_3)_6]$  (E = S, Se, Te) cluster molecules. *Dalton Trans.* **51**, 14568–14580 (2022).
- Hessen, B., Siegrist, T., Palstra, T., Tanzler, S. M. & Steigerwald, M. L. Hexakis(triethylphosphine)octatelluridohexachromium and a molecule-based synthesis of chromium telluride,  $\text{Cr}_3\text{Te}_4$ . *Inorg. Chem.* **32**, 5165–5169 (1993).
- Kiyoshi, T., Hideo, I. & Taro, S. Syntheses, structures, and molecular-orbital calculations of chromium Chevrel-type cluster complexes  $[\text{Cr}_6\text{E}_6(\text{PR}_3)_6]$  (E = S,  $\text{PR}_3 = \text{PET}_3, \text{PMe}_3$ ; E = Se,  $\text{PR}_3 = \text{PET}_3, \text{PMe}_3, \text{PMe}_2\text{Ph}$ ). *Bull. Chem. Soc. Jpn* **69**, 627–636 (1996).
- Kamiguchi, S., Imoto, H., Saito, T. & Chihara, T. Syntheses, structures, FAB mass spectra, and magnetic properties of chromium chalcogenide cluster complexes  $[\text{Cr}_6\text{Se}_6(\text{PET}_3)_6]$ ,  $[\text{Cr}_6\text{Se}_6(\text{H})(\text{PET}_3)_6]$ , and  $[\text{Cr}_6\text{S}_6(\text{H})(\text{PET}_3)_6]$ . *Inorg. Chem.* **37**, 6852–6857 (1998).
- Chaves, A. S., Piotrowski, M. J. & Da Silva, J. L. F. Evolution of the structural, energetic, and electronic properties of the 3d, 4d, and 5d transition-metal clusters (30  $\text{TM}_n$  systems for  $n = 2$ –15): a density functional theory investigation. *Phys. Chem. Chem. Phys.* **19**, 15484–15502 (2017).
- McGrady, J. E., Weigend, F. & Dehnen, S. Electronic structure and bonding in endohedral Zintl clusters. *Chem. Soc. Rev.* **51**, 628–649 (2022).
- Wilson, R. J., Lichtenberger, N., Weinert, B. & Dehnen, S. Intermetallic and heterometallic clusters combining  $p$ -block (semi)metals with  $d$ - or  $f$ -block metals. *Chem. Rev.* **119**, 8506–8554 (2019).
- Mayer, K., Wessing, J., Fässler, T. F. & Fischer, R. A. Intermetallic clusters: molecules and solids in a dialogue. *Angew. Chem. Int. Ed.* **57**, 14372–14393 (2018).
- Spiekermann, A., Hoffmann, S. D., Kraus, F. & Fässler, T. F.  $[\text{Au}_3\text{Ge}_6]^{5-}$ —a gold–germanium cluster with remarkable Au–Au interactions. *Angew. Chem. Int. Ed.* **46**, 1638–1640 (2007).
- Pan, F. X. et al. An all-metal aromatic sandwich complex  $[\text{Sb}_3\text{Au}_3\text{Sb}_3]^{3-}$ . *J. Am. Chem. Soc.* **137**, 10954–10957 (2015).
- Lips, F., Clerac, R. & Dehnen, S.  $[\text{Pd}_3\text{Sn}_8\text{Bi}_6]^{4-}$ : a 14-vertex Sn/Bi cluster embedding a  $\text{Pd}_3$  triangle. *J. Am. Chem. Soc.* **133**, 14168–14171 (2011).
- Perla, L. G., Muñoz-Castro, A. & Sevov, S. C. Eclipsed- and staggered- $[\text{Ge}_6\text{Pd}_3\{\text{E}^i\text{Pr}_3\}_6]^{2-}$  (E = Si, Sn): positional isomerism in deltahedral Zintl clusters. *J. Am. Chem. Soc.* **139**, 15176–15181 (2017).
- Perla, L. G. & Sevov, S. C. A stannyl-decorated Zintl ion  $[\text{Ge}_6\text{Pd}_3(\text{Sn}^i\text{Pr}_3)_6]^{2-}$ : twinned icosahedron with a common  $\text{Pd}_3$ -face or 18-vertex hypho-deltahedron with a  $\text{Pd}_3$ -triangle inside. *J. Am. Chem. Soc.* **138**, 9795–9798 (2016).
- Zhang, W. Q., Li, Z., McGrady, J. E. & Sun, Z. M. Synthesis and characterization of  $[\text{Fe}_3(\text{As}_3)_3\text{As}_4]^{3-}$ , a binary Fe/As Zintl cluster with an  $\text{Fe}_3$  core. *Angew. Chem. Int. Ed.* **62**, e202217316 (2023).
- Qiao, L. et al.  $[\text{Cu}_4\text{@E}_6]^{4-}$  (E = Sn, Pb): fused derivatives of endohedral stannaspherene and plumbaspherene. *J. Am. Chem. Soc.* **142**, 13288–13293 (2020).
- Eichhorn, B. W., Haushalter, R. C. & Huffman, J. C. Insertion of  $\text{Cr}(\text{CO})_3$  into As to form  $[\text{As}_7\text{Cr}(\text{CO})_3]^{3-}$ : an inorganic nortricyclane-to-norbornadiene conversion. *Angew. Chem. Int. Ed.* **28**, 1032–1033 (1989).
- Schiemenz, B. & Huttner, G. The first octahedral Zintl ion: Sn as a ligand in  $[\text{Sn}_6\{\text{Cr}(\text{CO})_5\}_6]^{2-}$ . *Angew. Chem. Int. Ed.* **32**, 297–298 (1993).
- Charles, S., Eichhorn, B. W., Rheingold, A. L. & Bott, S. G. Synthesis, structure, and properties of the  $[\text{E}_7\text{M}(\text{CO})_3]^{3-}$  complexes where E = P, As, Sb and M = Cr, Mo, W. *J. Am. Chem. Soc.* **116**, 8077–8086 (1994).
- Kesanli, B., Fettingner, J. & Eichhorn, B. The *closo*- $[\text{Sn}_9\text{M}(\text{CO})_3]^{4-}$  Zintl ion clusters where M = Cr, Mo, W: two structural isomers and their dynamic behavior. *Chem. Eur. J.* **7**, 5277–5285 (2001).
- Renner, G., Kircher, P., Huttner, G., Rutsch, P. & Heinze, K. Efficient syntheses of the complete set of compounds  $\{[(\text{OC})_5\text{M}]_6\text{E}_6\}^{2-}$  (M = Cr, Mo, W; E = Ge, Sn)—structure and redox behaviour of the octahedral clusters  $[\text{Ge}_6]^{2-}$  and  $[\text{Sn}_6]^{2-}$ . *Chem. Eur. J.* **2001**, 973–980 (2001).
- Geitner, F. S., Klein, W. & Fässler, T. F. Synthesis and reactivity of multiple phosphine-functionalized nonagermanide clusters. *Angew. Chem. Int. Ed.* **57**, 14509–14513 (2018).
- Huang, Y.-S., Chen, D., Zhu, J. & Sun, Z.-M.  $[(\text{CrGe}_9)\text{Cr}_2(\text{CO})_{13}]^{4-}$ : a disubstituted case of ten-vertex *closo* cluster with spherical aromaticity. *Chin. Chem. Lett.* **33**, 2139–2142 (2022).
- Mondal, S., Chen, W.-X., Sun, Z.-M. & McGrady, J. E. Synthesis, structure and bonding in pentagonal bipyramidal cluster compounds containing a *cyclo*- $\text{Sn}_5$  ring,  $[(\text{CO})_3\text{MSn}_5\text{M}(\text{CO})_3]^{4-}$  (M = Cr, Mo). *Inorganics* **10**, 75 (2022).
- Schenk, C. & Schnepf, A.  $\{\text{Ge}_9\text{R}_3\text{Cr}(\text{CO})_5\}^-$  and  $\{\text{Ge}_9\text{R}_3\text{Cr}(\text{CO})_3\}^-$ : a metalloid cluster ( $\text{Ge}_9\text{R}_3^-$ ) as a flexible ligand in coordination chemistry [R = Si( $\text{SiMe}_3$ )<sub>3</sub>]. *Chem. Commun.* 3208–3210 (2009).
- Yang, Y.-N. et al. Metal–metal bonds in Zintl clusters: synthesis, structure and bonding in  $[\text{Fe}_2\text{Sn}_4\text{Bi}_6]^{3-}$  and  $[\text{Cr}_2\text{Sb}_{12}]^{3-}$ . *Chin. Chem. Lett.* **35**, 109048 (2024).
- Min, X. et al. All-metal antiaromaticity in  $\text{Sb}_4$ -type lanthanocene anions. *Angew. Chem. Int. Ed.* **55**, 5531–5535 (2016).
- Lichtenberger, N. et al. Main group metal–actinide magnetic coupling and structural response upon  $\text{U}^{4+}$  inclusion into Bi, Tl/Bi, or Pb/Bi cages. *J. Am. Chem. Soc.* **138**, 9033–9036 (2016).
- Eulenstein, A. R. et al. Substantial  $\pi$ -aromaticity in the anionic heavy-metal cluster  $[\text{Th@Bi}_{12}]^{4-}$ . *Nat. Chem.* **13**, 149–155 (2021).

52. Wang, Y. et al.  $\text{Sb@Ni}_{12}\text{@Sb}_{20}^{-/+}$  and  $\text{Sb@Pd}_{12}\text{@Sb}_{20}^n$  cluster anions, where  $n = +1, -1, -3, -4$ : multi-oxidation-state clusters of interpenetrating platonic solids. *J. Am. Chem. Soc.* **139**, 619–622 (2017).
53. Chen, W.-X. et al. Fe–Fe bonding in the rhombic  $\text{Fe}_4$  cores of the Zintl clusters  $[\text{Fe}_4\text{E}_{18}]^{4-}$  (E = Sn and Pb). *Chem. Sci.* **15**, 4981–4988 (2024).
54. Scott, A. G. et al. High-spin and reactive  $\text{Fe}_{13}$  cluster with exposed metal sites. *Angew. Chem. Int. Ed.* **62**, e202313880 (2023).
55. Beekman, M., Kauzlarich, S. M., Doherty, L. & Nolas, G. S. Zintl phases as reactive precursors for synthesis of novel silicon and germanium-based materials. *Materials* **12**, 1139 (2019).
56. Myers, A. G., Sogi, M., Lewis, M. A. & Arvedson, S. P. Synthetic and theoretical studies of cyclobuta[1,2:3,4]dicyclopentene. Organocobalt intermediates in the construction of the unsaturated carbon skeleton and their transformation into novel cobaltacyclic complexes by C–C insertion. *J. Org. Chem.* **69**, 2516–2525 (2004).
57. Eisenmann, B. & Klein, J.  $\text{Na}_5\text{SnSb}_3$  und  $\text{K}_8\text{SnSb}_4$ , zwei neue Zintlphasen mit tetraedrischen  $\text{SnSb}_4$ -Baueinheiten. *Z. Naturforsch. B* **43**, 1156–1160 (1988).
58. Spreer, L. O. & Shah, I. Evidence for a novel  $\pi$ -bonded aquoorganochromium(III) ion,  $(\eta^5\text{-C}_5\text{H}_5)\text{Cr}(\text{OH})_2\text{H}_2^+$ . *Inorg. Chem.* **20**, 4025–4027 (1981).
59. Sheldrick, G. M. SHELXT—integrated space-group and crystal-structure determination. *Acta Crystallogr. A* **71**, 3–8 (2015).
60. Dolomanov, O. V., Bourhis, L. J., Gildea, R. J., Howard, J. A. K. & Puschmann, H. OLEX2: a complete structure solution, refinement and analysis program. *J. Appl. Crystallogr.* **42**, 339–341 (2009).
61. Spek, A. L. Structure validation in chemical crystallography. *Acta Crystallogr. D* **65**, 148–155 (2009).
62. Spek, A. L. PLATON SQUEEZE: a tool for the calculation of the disordered solvent contribution to the calculated structure factors. *Acta Crystallogr. C* **71**, 9–18 (2015).
63. Frisch, M. J. et al. *Gaussian 16, Revision A.03* (Gaussian Inc., 2016).
64. Weigend, F. & Ahlrichs, R. Balanced basis sets of split valence, triple zeta valence and quadruple zeta valence quality for H to Rn: design and assessment of accuracy. *Phys. Chem. Chem. Phys.* **7**, 3297–3305 (2005).
65. Zubarev, D. Y. & Boldyrev, A. I. Developing paradigms of chemical bonding: adaptive natural density partitioning. *Phys. Chem. Chem. Phys.* **10**, 5207–5217 (2008).
66. Lu, T. & Chen, F. Multiwfn: a multifunctional wavefunction analyzer. *J. Comput. Chem.* **33**, 580–592 (2012).
67. Mitoraj, M. P., Michalak, A. & Ziegler, T. Combined charge and energy decomposition scheme for bond analysis. *J. Chem. Theory Comput.* **5**, 962–975 (2009).
68. Velde, G. et al. Chemistry with ADF. *Comput. Chem.* **22**, 931–967 (2001).
69. Lenthe, E., Baerends, E. J. J. & Snijders, J. G. Relativistic total energy using regular approximations. *Chem. Phys.* **101**, 9783–9792 (1994).
70. Chang, C., Pelissier, M. & Durand, P. Regular two-component Pauli-like effective Hamiltonians in Dirac theory. *Phys. Scr.* **34**, 394 (1986).
71. Heully, J. L., Lindgren, I., Lindroth, E., Lundqvist, S. & Martensson-Pendrill, A. M. Comment on the relativistic wave equation and negative-energy states. *Phys. Rev. A* **33**, 4426–4429 (1986).
72. Zhao, L., Pan, S. & Frenking, G. Energy decomposition analysis of the chemical bond: scope and limitation. *Compr. Comput. Chem.* **2**, 322–361 (2024).
73. Zhao, L., von Hopffgarten, M., Andrada, D. M. & Frenking, G. Energy decomposition analysis. *Wiley Interdiscip. Rev. Comput. Mol. Sci.* **8**, e1345 (2018).
74. Frisch, M. J. et al. *Gaussian 09, Revision D.01* (Gaussian Inc., 2009).
75. Klamt, A. & Schüürmann, G. COSMO: a new approach to dielectric screening in solvents with explicit expressions for the screening energy and its gradient. *J. Chem. Soc. Perkin Trans. 2* **105**, 799–805 (1993).

## Acknowledgements

This work was supported by the National Natural Science Foundation of China (grant nos. 22425107, 92461303, 22371140 and 92161102 to Z.-M.S and grant no. 22402108 to W.-J.T.), the Natural Science Foundation of Tianjin City (grant no. 21JCZJJC00140), the China Postdoctoral Science Foundation under Grant Number 2024M761514 and 111 Project of China (MOE, B18030). A.M.-C. thanks ANID FONDECYT Regular 1221676 for financial support.

## Author contributions

Z.-M.S. conceived the project and designed the experiments. W.-X.C. conducted the syntheses. W.-J.T., Z.-S.L., J.-J.W., A.M.-C. and G.F. performed the quantum chemical calculations and analysed the data. Z.-M.S., W.-X.C., W.-J.T. and A.M.-C. co-wrote the paper. All authors reviewed the paper.

## Competing interests

The authors declare no competing interests.

## Additional information

**Supplementary information** The online version contains supplementary material available at <https://doi.org/10.1038/s44160-024-00711-5>.

**Correspondence and requests for materials** should be addressed to Zhong-Ming Sun.

**Peer review information** *Nature Synthesis* thanks Jorge Barroso and the other, anonymous, reviewer(s) for their contribution to the peer review of this work. Primary Handling Editor: Alexandra Groves, in collaboration with the *Nature Synthesis* team.

**Reprints and permissions information** is available at [www.nature.com/reprints](http://www.nature.com/reprints).

**Publisher's note** Springer Nature remains neutral with regard to jurisdictional claims in published maps and institutional affiliations.

Springer Nature or its licensor (e.g. a society or other partner) holds exclusive rights to this article under a publishing agreement with the author(s) or other rightsholder(s); author self-archiving of the accepted manuscript version of this article is solely governed by the terms of such publishing agreement and applicable law.

© The Author(s), under exclusive licence to Springer Nature Limited 2025